PCCP

PAPER

View Article Online
View Journal | View Issue

Check for updates

Cite this: *Phys. Chem. Chem. Phys.*, 2022, **24**, 18729

Structure–property investigations in urea tethered iodinated triphenylamines†

Muhammad Saddam Hossain,[a] Fiaz Ahmed,[a] Stavros G. Karakalos,[b] Mark D. Smith,[a] Namrata Pant,[c] Sophya Garashchuk,[a] Andrew B. Greytak,[a] Pablo Docampo[c] and Linda S. Shimizu*[a]

Herein, we report structural, computational, and conductivity studies on urea-directed self-assembled iodinated triphenylamine (TPA) derivatives. Despite numerous reports of conductive TPAs, the challenges of correlating their solid-state assembly with charge transport properties hinder the efficient design of new materials. In this work, we compare the assembled structures of a methylene urea bridged dimer of di-iodo TPA (**1**) and the corresponding methylene urea di-iodo TPA monomer (**2**) with a di-iodo mono aldehyde (**3**) control. These modifications lead to needle shaped crystals for **1** and **2** that are organized by urea hydrogen bonding, π···π stacking, I···I, and I···π interactions as determined by SC-XRD, Hirshfeld surface analysis, and X-ray photoelectron spectroscopy (XPS). The long needle shaped crystals were robust enough to measure the conductivity by two contact probe methods with **2** exhibiting higher conductivity values ($\sim 6 \times 10^{-7}$ S cm^{-1}) compared to **1** (1.6×10^{-8} S cm^{-1}). Upon UV-irradiation, **1** formed low quantities of persistent radicals with the simple methylurea **2** displaying less radical formation. The electronic properties of **1** were further investigated using valence band XPS, which revealed a significant shift in the valence band upon UV irradiation (0.5–1.9 eV), indicating the potential of these materials as dopant free p-type hole transporters. The electronic structure calculations suggest that the close packing of TPA promotes their electronic coupling and allows effective charge carrier transport. Our results show that ionic additives significantly improve the conductivity up to $\sim 2.0 \times 10^{-6}$ S cm^{-1} in thin films, enabling their implementation in functional devices such as perovskite or solid-state dye sensitized solar cells.

Received 22nd April 2022,
Accepted 15th July 2022

DOI: 10.1039/d2cp01856j

rsc.li/pccp

Open Access Article. Published on 18 July 2022. Downloaded on 5/10/2026 2:54:14 PM.
This article is licensed under a Creative Commons Attribution 3.0 Unported Licence.

Introduction

Intentional design of supramolecular frameworks can lead to the emergence of properties such as new magnetic,[1] dichroic,[2] or conductive properties.[3] Triphenylamine (TPA) is a redox-active organic molecule that can generate electron/hole pairs and has been widely used as a hole transporter in the semiconductor industry[4] and has applications in dye-sensitized solar cells,[5] perovskite solar cells,[6] organic light-emitting diodes (OLEDs),[7] fluorescence imaging,[8] and magnetic materials.[9] Incorporation of TPA into self-assembled materials can modify their electronic structure and generate pronounced effects on their functional properties. For instance, Giuseppone and co-workers reported TPA-based self-assembled supramolecular conductive nanowires, which have applications as liquid crystals and metallic interconnects.[10–12] Recently, much effort has been focused on developing TPA based hole transporting materials for next-generation organic solar cells.[13–15] Overall, a greater understanding of how the TPA structure and its controlled assembly correlate with electronic properties would facilitate design of better hole transporters. Yet, full characterization of solid-state assemblies of TPA derivatives remains a challenge. Thus, strategies that direct high fidelity assembly of TPAs and enable the investigation of the structure with respect to conductivity and electron–hole pair generation are important for the development of these functional materials.

Non-covalent interactions contribute to crystal packing and can tune assembled functional materials from semiconductors to conductors.[16–18] Constructing non-covalent interactions to control the organization of tethered TPAs must take into account their structure and conformations. The phenyl rings of TPA are arranged in propeller shapes, making a halo of the π

[a] *Department of Chemistry and Biochemistry, University of South Carolina, Columbia, South Carolina 29208, USA. E-mail: SHIMIZLS@mailbox.sc.edu*
[b] *College of Engineering and Computing, University of South Carolina, Columbia, South Carolina 29208, USA*
[c] *School of Chemistry, University of Glasgow, Joseph Black building, University pl., Glasgow, G12 8QQ, UK*

† Electronic supplementary information (ESI) available: Experimental details; synthesis and characterization; SC-XRD data, absorption, and emission, ^{1}H NMR, conductivity data, and TD-DFT calculations. CCDC 2165898–2165901. For ESI and crystallographic data in CIF or other electronic format see DOI: https://doi.org/10.1039/d2cp01856j

Open Access Article. Published on 18 July 2022. Downloaded on 5/10/2026 2:54:14 PM.
This article is licensed under a Creative Commons Attribution 3.0 Unported Licence.

orbitals electrons above and below the molecular plane, which facilitate the transfer of the charge carriers.[19] This effect can be extended through π–π or halogen–π interactions. These modifications also increase the solution processability of TPA derivatives in thin-films.[20,21] Indeed, there is strong interest in solution-based processes (*e.g.* spin coating, ink-jet or gravure printing or slot-die coating) as these can be deposited cheaply and with high throughput employing conventional printing equipment.[22–24]

Single crystal X-ray diffraction (SC-XRD) techniques can be employed to extract structural information for correlation with functional features. Osman and coworkers recently crystallized TPA-based Spiro-OMeTAD *via* the anti-solvent method and employed it as a hole transfer layer in perovskite solar cells. They have observed that mesoscale ordering driven by discontinuous π–π stacking interactions between the fluorene plane of adjacent Spiro-OMeTAD is essential for transporting the charges.[25] In Giuseppone's crystalline amide appended TPA derivatives,[26] SC-XRD data suggest the formation of equidistant snowflake conformations packed *via* intercolumnar hydrogen bonds. Higher mobilities of charges were observed in these crystals, which was attributed to the tight packing of the aromatic cores between stacked dimers. While most of the prior designs relied on assemblies *via* the phenyl core, our effort to control TPA assembly relies on the bifurcated urea hydrogen bonding, halogen bonding and halogen–π interactions. Herein, a tetra-iodinated **1** and urea tethered di-iodinated **2** are synthesized and crystallized. These structures incorporate iodine on the *para* positions of the external phenyl rings (Fig. 1(b)). While urea hydrogen bonding guides the assembly, the close packing of TPA units is further tailored by I–I, π–π, and I–π interactions. These crystalline materials form low levels of radicals upon prolonged UV-irradiation. The photophysics, conductivity, and ion mobility of these materials were explored in thin films and crystals. In addition, computational approaches were used to probe the electron transport in these systems.

The Shimizu group utilizes urea to guide the assembly of macrocycles and linear dimers to afford needle shaped crystals which are readily characterized by SC-XRD.[27–29] Previously, a series of urea tethered TPA derivatives with one of the *para* positions of the phenyl groups modified with a halogen has been examined.[30] Assembled, these materials were surprisingly stable and could generate stable radicals with variable quantities. These studies found that the bromo derivative generated the highest percentage of radicals while the iodo derivative formed the least. According to Time-dependent Density Functional Theory (TD-DFT) calculations, the electronic coupling in the hydrogen-bonded dimers of the iodo derivative was 7 times stronger as compared to that of the bromo derivative. The stronger computed coupling suggested that these materials might have better conductivity; however, the crystals were small and spherical shaped. We hypothesized that complete iodine substitution on the external phenyl rings would increase the electronic coupling, facilitate organization of the TPA units by halogen bonding interactions, and afford larger crystals. To test this hypothesis, urea tethered tetra-iodinated **1** and di-iodinated **2** were synthesized and crystallized, forming crystals (50–200 μm). Their SC-XRD determined structures were compared with that of control **3** to investigate the effect of urea tethering and iodine substitution on the 3-dimensional structures. Hirshfeld surface analysis and XPS studies suggest that urea guided the assembled TPA units into tapes, which then closely packed *via* C–I···π, I–I interactions. The conductivity of a single crystal was measured *via* the two-contact probe method. TD-DFT was used to investigate the electron transfer mechanism within hydrogen-bonded stacks which aids in correlating the structure with the function. Finally, conductivity for **1** was tested in thin films and compared with that of the popular hole transporting material Spiro-OMeTAD.

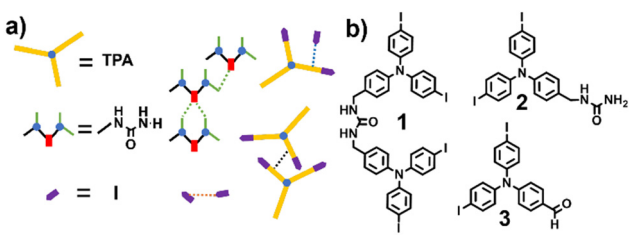

Fig. 1 (a) Schematic of non-covalent interactions for organizing linear triphenylamine (TPA) include intra/intermolecular hydrogen bond (green), I–I halogen bond (orange), I–π interactions (blue), offset π–π stacking interaction (black). (b) Comparison of TPA structures investigated. TPA tethered to both side of urea **1**. TPA tethered to one side of urea **2**. TPA **3** lacking the urea assembly motif.

Experimental methods

Synthesis and crystallization

Urea tethered iodinated TPAs **1** and **2** were synthesized in six steps (Scheme S1, ESI†).[30] A Vilsmeier–Haack reaction converted commercial TPA to its mono aldehyde.[31] Iodination of the remaining phenyl rings was carried out with potassium iodide and potassium iodate to yield **3**.[32] A modified reductive amination with urea yields a single TPA tethered to methylene urea **2**. Alternatively, the aldehyde was reduced to alcohol.[33] Bromination followed by subsequent reaction with triazinanone under basic conditions yields the urea tethered dimer.[34] Deprotection was performed in a mixture of 9 : 1 DMF/DEA (diethanolamine) in acidic medium to yield **1**. X-ray diffraction quality ethyl acetate or methanol solvated crystals of **1** were obtained by slow evaporation either from ethyl acetate (2.5 mg mL^{-1}) or a 1 : 1 mixture of DCM:methanol solution (5 mg mL^{-1}). Solvent-free crystals of **2** were obtained by slow evaporation from ethyl acetate (2.5 mg mL^{-1}). The yellow plate crystals of **3** were obtained by slow evaporation of 1 : 1 = DCM : hexane (5 mg mL^{-1}).

Physical measurements

Single crystal X-ray diffraction (SCXRD) analysis details are given in the ESI.† A Waveform Lighting Real UV 365 nm LED

 This journal is © the Owner Societies 2022

Open Access Article. Published on 18 July 2022. Downloaded on 5/10/2026 2:54:14 PM.
This article is licensed under a Creative Commons Attribution 3.0 Unported Licence.

system was used for UV irradiation. UV/Vis absorption spectra in solution were recorded on Spectramax M2 from Molecular Devices. Diffuse reflectance experiment of the solid sample was performed by using a PerkinElmer Lambda 45 UV/vis spectrometer using UV Winlab software and Spectralon®. The emission experiment in solution (cuvette) was carried out using a PerkinElmer LS55 fluorescence spectrometer equipped with a pulsed high-energy source for excitation. Photoluminescence experiments on solid samples were performed using a HORIBA Micro-SPEX system equipped with an iHR320 spectrometer and Synchrony detector operated using Labspec 6 software. Spectra were recorded using a 375 nm laser excitation source with power delivery of 0.3 mW focused through a 10× UV objective. UV-irradiation and EPR experiments were conducted using Norell Suprasil Quartz tubes. The samples were sealed in these tubes under the protection of Ar(g). A Bruker EMX plus equipped with a Bruker X-band microwave bridgehead and Xenon software (v 1.1b.66) were used for EPR experiments. Double integration of the EPR spectra was performed using Xenon software to obtain the peak area. A Kratos AXIS Ultra DLD XPS system with a monochromatic Al Kα source, operated at 15 keV and 150 W and at pressures below 10^{-9} Torr was used for XPS analysis. The X-rays were incident at an angle of 45° with respect to the surface normal. High resolution core level spectra were measured with a pass energy of 40 EV and analysis of the data was carried out using XPSPEAK41 software. The XPS system was equipped with a hemispherical electron analyzer and a load lock chamber for rapid introduction of samples without breaking the vacuum. The XPS experiments were conducted using an electron gun, directed on the sample for charge neutralization. The UV irradiation took place *in situ*, through the windows of the Ultra High Vacuum chamber.

Computations

TD-DFT was used to analyze the electronic excitations. All calculations were performed using Q-Chem 5.3[35] and Spartan18.[36] The basis set exchange was used for the selected bases.[37] SC-XRD data (positions of heavy atoms) were used to construct the cluster models for the calculations performed in the gas phase. The B3LYP-D3[38]/6-31G*[39] theory level was employed to optimize the positions of all hydrogen atoms. The TD-DFT calculations are based on the CAM-B3LYP[40] functional paired with the effective core potential basis LANL2DZdp.[41] The theoretical UV-vis spectra were generated as sums of Gaussian functions, broadening the spectral lines as given by eqn (S1) (ESI,† eqn. (S1)). The broad feature of the experimental spectra was matched by standard deviation parameter σ set to 25. The frontier molecular orbitals (HOMO and LUMO) and the natural transition orbitals (HONTO and LUNTO) were visualized using IQmol v2.14.0 with the isovalue 0.04.

The electronic couplings for the dimer model were calculated in the ground state by using Koopmans' theorem. The neutral system's energy gap $E^{\mathrm{LUMO+1}} - E^{\mathrm{LUMO}}$ is proportional to twice the coupling between the initial and final states of an anionic dimer upon electron transfer. The coupling was computed within the Hartree–Fock theory paired with polarized bases def2-SVP.[42]

Results and discussion

Urea directed assembly of TPA

The colorless needle shaped crystals of **1** ethyl acetate solvate and plates of its methanol solvate were isostructural, despite their different forms. Both the solvated crystals of **1** crystallized in the triclinic space group $P\bar{1}$ (No. 2). The asymmetric unit consists of half each of two crystallographically independent TPA **1** molecules. A region of disordered ethyl acetate or methanol molecules is located on a crystallographic inversion center as shown in Fig. S6 and S7 (ESI†). Overall, the crystal consists of a 50/50 disorder of chains with urea groups pointing up or down while the rest of the group atoms remains the same. The TPAs on the opposite side of the urea arranged themselves in an inverted fashion with intra-molecule TPA N···N distances of 13.82 Å and 14.26 Å; along the chain (inter-molecular) 5.73 Å and 6.32 Å for two independent molecules (ethyl acetate solvated), slightly higher compared with the series of related compounds reported previously.[30] The ureas adopt the *trans–trans* conformation and typical three centered urea–urea hydrogen bonding directs the assembly with *d*(N···O) distances from 2.915(10)–3.152(12), Å and a twisting angle 27.16° (Fig. S11a, ESI†). The twisted chains of the ureas form a skewed shape if viewed along with the crystallographic *a*-axis (Fig. S11b, ESI†). Infinite 1D chains of H-bonded urea organize into columnar tubes that encapsulate ethyl acetate or methanol in host–guest ratios of 1 : 0.72 and 1 : 2 respectively as seen in Fig. 2(c), (d) and Fig. S11c (ESI†). The channel diameter of the interior cross-section is 7.18 × 3.64 Å centroid to centroid (Fig. 2(e)). Multiple face-to-face intermolecular π-stacking and C–I···π interactions are present within the channel (Fig. S13 and S14, ESI†). The neighboring tubes are held together by weak I···I halogen bonds (I···I distance 3.874 Å), slightly lower than the sum of van der Waals radii (3.96 Å) of iodine (Fig. S15, ESI†).[43]

The methylene urea **2** also crystallized in the triclinic space group $P\bar{1}$ (No. 2) with two crystallographically independent but chemically identical molecules in the asymmetric unit (Fig. S8, ESI†). Again, the ureas adopt the *trans–trans* conformation and urea hydrogen bonding directs the assembly with *d*(N···O) distances from 2.921(2) to 3.252(2) Å and a twisting angle of 17.81° (Fig. S12, ESI†). In addition, one urea NH hydrogen forms another hydrogen bond with a neighboring carbonyl oxygen (*d*(N···O) = 3.068(3) Å) to link two chains together (Fig. 2(b)). The individual chains are held together with weak I···I halogen bonds of length 3.854 Å, which is less than the sum of van der Waals radii (3.96 Å) as seen in Fig. S17 (ESI†). The control **3** aldehyde, with no hydrogen bonding groups, crystallized in the monoclinic system with the monoclinic space group *Pc*. The structure is disordered with the formyl group and iodines scrambled on two separate sites (Fig. S9, ESI†).

Giuseppone and others hypothesize that the relative orientation of TPA units are important for conductivity and photophysical properties of TPA supramolecular polymers.[10,44] Giuseppone and co-workers observed the stacking of TPA units with favourable snowflake or Mercedes-Benz conformation

Open Access Article. Published on 18 July 2022. Downloaded on 5/10/2026 2:54:14 PM.
This article is licensed under a Creative Commons Attribution 3.0 Unported Licence.

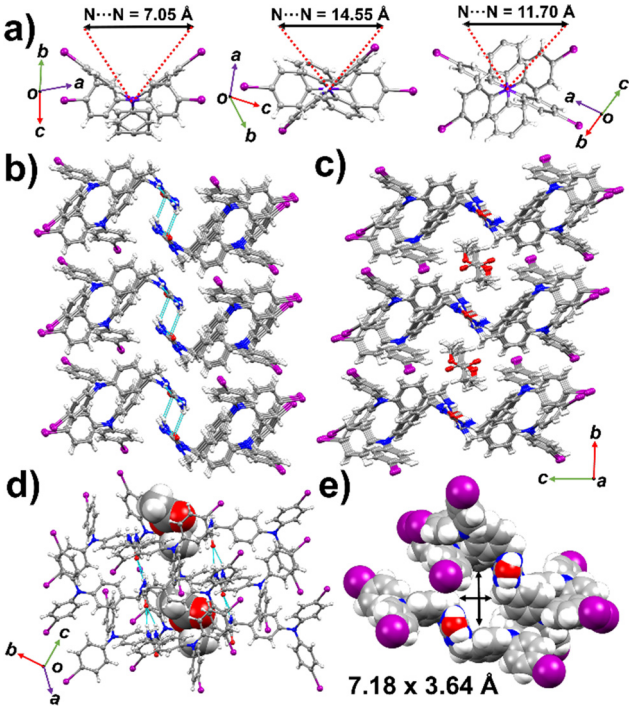

Fig. 2 Comparison of urea tethered solvated crystal **1**, urea tethered solvent free crystal **2**, crystals of **3**. Disorder omitted for clarity. (a) Packing of TPA units in **3** (left), **2** (middle), **1** (right). (b) Assembly of **2** through hydrogen-bonded urea tape. Inter-chain H-bonds links two strands (top down view). (c) Packing of **1** through hydrogen-bonded urea tape. H-bonded urea chains encapsulate ethyl acetate. (d) A view of bifurcated H-bond chain running parallel to crystallographic *a* axis in **1**. Ethyl acetate molecules are shown in the spacefill model. (e) Spacefill model of **1** showing the cross-sectional area of the channel. (vdW radii subtracted).

with N···N distances of 4.8 Å to 5 Å. Therefore, the packing of TPA units in **1–3** was analysed from this perspective. In both solvated crystal forms of **1**, the TPAs adopt a slightly rotated snowflake conformation (Fig. 2(a), right) with the intermolecular TPA N–N distance 11.70 Å. The TPA units of **2** organized into a cross-flake conformation (Fig. 2(a), middle) with intermolecular TPA N···N distances of 14.55 Å. Aldehyde **3** (Fig. 2(a), left) forms a butterfly shape with intermolecular TPA N···N distances of 7.05 Å. The phenyl rings of **3** exhibits a less rotated conformation (51.76–62.11°) compared to **2** (71.54–93.55°), and **1** (64.06–75.56°) as seen in Fig. S10 (ESI†).

Hirshfeld surface analysis was utilized to further investigate the non-covalent interaction promoting the packing of the crystals of **1** and **2**.[45] Hirshfeld surface mapping (Fig. 3(a) and (b)) of **1** and **2** shows the key urea hydrogen bonding interaction indicated in red. We observed offset π stacking interactions in **2** with distances 3.023 Å and 3.597 Å measured from H – centroid. There are C–I···π (3.881 Å), and offset π stacking (3.135 Å) interactions in **1** suggested by the Hirshfeld surface analysis. X-ray photoelectron spectroscopy (XPS) was further utilized to probe the chemical environment around the iodine. A shift in the binding energy of the core level electrons of I(3d) would be expected due to the interactions of C–I···π and I···I halogen bonds. Indeed, a shift was observed in the binding energy I(3d)

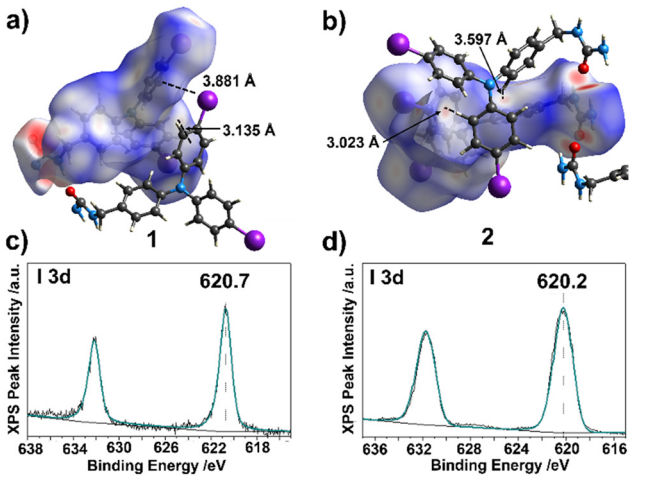

Fig. 3 Hirshfeld surface map (Isovalue 0.05) and I(3d) XPS core level peaks recorded with a monochromatic Al Kα X-ray source of the asymmetric unit of **1** and **2**. (a) Hirshfeld surface map of **1** showing C–I···π, and offset π stacking interactions. (b) Hirshfeld surface map of **2** showing offset π stacking interactions. (c) I(3d) XPS core level peaks for **1** (ethyl acetate solvated). (d) I(3d) XPS core level peaks for **2**.

from 619 eV to 620.7 eV and 620.2 eV for **1** (ethyl acetate solvated), and **2** respectively (Fig. 3(c) and(d)), corresponding to halogen bonding previously characterized by our group.[46,47] These results suggest that urea directed assembly was further promoted by close packing of TPA units.

Photophysical properties

To probe how assembly and packing of TPA units effects the photophysics in the solid-state, diffuse reflectance and photoluminescence experiments were performed for each sample (Table S2, ESI†). Diffuse reflectance experiments on bulk crystals (Fig. S18, ESI†) show that the absorbance of urea containing materials **1** and **2** were shifted to the lower wavelength 361 nm and 367 nm respectively as compared to **3** at 445 nm, which has longer conjugation. The absorbance of **1** was also studied in thin films and in solution (argon purged methylene chloride) at room temperature (Fig. S19, ESI†). The absorbance was observed at shorter wavelength at 321 nm (thin films) and 309 nm (solution) as compared to the bulk crystals. A photoluminescence study was done on single crystals of **1–3** using λ_{EXC} = 375 nm (Fig. S20, ESI†). The emission bands ranged from 451 to 503 nm with **2** exhibiting the longer wavelength emission λ_{Em} = 503 and a larger Stokes shift (136 nm) as compared to **1** λ_{Em} = 451 nm (Stokes shift ~90 nm). The aldehyde **3** in comparison showed λ_{Em} = 478 nm with a Stokes shift of 33 nm. Packing has been shown to influence the photophysics in di-halogenated methylene urea derivatives with smaller twisting angle shows a higher Stokes shift.[30] Higher, red-shifted emissions were also observed for the formation of the excimer due to closely packed TPA units.[48] The emission study of **1** in solution (10 μM in dry CH_2Cl_2) displayed two bands at 365 nm and 440 nm, while a quenching study in oxygen purged solution suggest that both the bands may arise due to fluorescence (Fig. S21, ESI†).

 This journal is © the Owner Societies 2022

Open Access Article. Published on 18 July 2022. Downloaded on 5/10/2026 2:54:14 PM.
This article is licensed under a Creative Commons Attribution 3.0 Unported Licence.

Conductivity measurements

The intrinsic electrical conductivity of the single crystal of **1** and **2** were measured using a 2-contact probe method at room temperature (Fig. 4). For the measurement, triply recrystallized samples were used (see the ESI† for further details of the experimental setup). The total resistance was obtained by fitting the linear region of a current–voltage (*I–V*) curve using Ohm's law. The applied voltage was swept over ±10 V, and samples were measured in the dark. The calculated electrical conductivity of three different trials of single crystals of **1** and **2** tabulated in Tables S3 and S4 (ESI†). The highest electrical conductivity of a single crystal of **1** is 1.65×10^{-8} S cm^{-1} and in a range of 1.41×10^{-9} to 1.65×10^{-8} S cm^{-1}. TPA **2** shows a higher conductivity value compared to **1** with the highest conductivity 6.44×10^{-7} S cm^{-1} and in a range of 6.44×10^{-7} S cm^{-1} to 2.93×10^{-10} S cm^{-1}. Dimensions and morphology of the crystal (cracked or twisted) can influence the conductivity as in the case of **2** in which much thinner crystals displayed very low conductivity. The electrical conductivity of **1** was performed on the ethyl acetate solvated crystal, which could partially explain lower conductivity values compared to **2**. It should be noted that most of the higher conductivity values for the TPA derivatives were observed in thin films, which was attributed to close packing and enhanced stacking interaction of phenyl rings.[6]

Our previous work on halogen-substituted urea tethered TPA derivatives suggested the formation of low amounts of radicals upon UV irradiation.[30] However, it was not clear whether radical formation would be beneficial or detrimental to conductivity. In those prior systems, the partial iodine substituted urea tethered TPA derivative exhibited the highest electronic coupling as well as the least radical formation. We expected that complete iodine substitution would further enhance electronic coupling as facilitated by close packing of TPA units. To further investigate the effect of light, the conductivity of **1** and **2** were measured upon UV irradiation (Tables S5 and S6, ESI†). For the experiments, 365 nm UV LED was used (photon flux 4.26×10^{14} photons per second) and conductivity was measured at time intervals between 0 and 5 h. Upon UV-irradiation a reduction of conductivity was observed for both **1** and **2** which plateaued at 5 hours (Fig. 4(c) and (d)). The single crystal of **1** shows higher sensitivity upon UV irradiation as the conductivity decreases by ~69% compared to **2** (~33%). To test whether the conductivity of crystal **1** reverts to its initial state, the conductivity of the sample was continuously monitored in the dark after initial 5 hours of UV irradiation (Table S7, ESI†). No significant change in the conductivity value of **1** was observed over this time (Fig. S22, ESI†). Our hypothesis is that UV irradiation promotes long-lived electron transfers, further evidenced by the appearance of unpaired spins as discussed below, that act to decrease the electrical conductivity by compensating acceptors and/or diminishing hole mobility through increased scattering.[25,49]

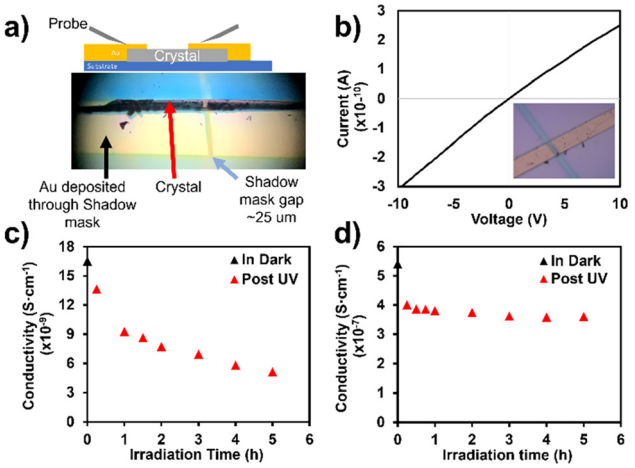

Fig. 4 Electrical conductivity measurement under dark and UV-irradiation at room temperature. (a) two contact probe setup used to measure the conductivity of a single crystal (shadow mask gap 25 μm). (b) *I–V* curve for a trial of **1** under dark at room temperature by measuring the sum of resistance of the material, wires, and contacts using two contact probe method. Inset shows a single crystal setup. (c) and (d) changes in electrical conductivity under UV-irradiation using 365 nm UV sources at room temperature for **1** and **2** respectively.

The thin film conductivity of **1** was investigated to understand the behaviour and potential of these materials as charge transporting materials (CTM) in optoelectronic devices such as perovskite solar cells (PSCs). The conductivity was measured in a 'sandwich' architecture, *i.e.* a vertical stack of ITO/HTM/Au. The films were deposited *via* spin coating from chlorobenzene and chloroform mixtures with additives; see details in the ESI.† Here, we note that to maximize the performance of developed materials, it is standard practice to include ionic additives to improve their conductivity *via* oxygen-induced p-doping. We compare our material with the state-of-the-art TPA-based hole transporting material (HTM) termed 'Spiro-OMeTAD' in the literature which is typically doped with (lithium bis(trifluoromethanesulfonyl)imide (LiTFSI) and 4-*tert*-butylpyridine (tBP)).[50,51] While LiTFSI favors the oxidation and hence the p-doping of Spiro-OMeTAD,[52] tBP molecules have been shown to prevent LiTFSI aggregation, improve its distribution within the film and to provide a better interface between the HTM layer and the perovskite layer.[53] The conductivity of these films was measured in the dark. Fig. 5 shows representative *I–V* curves for **1** (65 nm) and Spiro-OMeTAD (300 nm), indicating linear relationships. The conductivity value obtained for Spiro-OMeTAD ($(0.8 \pm 0.1) \times 10^{-6}$ S cm^{-1}) was in the range reported in the literature for this material which lies between 10^{-5} and 10^{-8} S cm^{-1} depending on the additive concentration, oxidation time, and environmental conditions.[54] Interestingly, **1** demonstrated similar conductivity values ($(2 \pm 1) \times 10^{-6}$ S cm^{-1}) as Spiro-OMeTAD under the same conditions, highlighting its potential as an alternative suitable choice for HTMs in perovskite/solid-state dye solar cells.

EPR experiments

To further probe the effect of UV irradiation, the crystals were examined by X-band EPR spectroscopy. This technique enabled measurement of radical formation in **1** and **2** *versus* UV-irradiation time (0–16 h) with the 365 LEDs (photon flux

Open Access Article. Published on 18 July 2022. Downloaded on 5/10/2026 2:54:14 PM.
This article is licensed under a Creative Commons Attribution 3.0 Unported Licence.

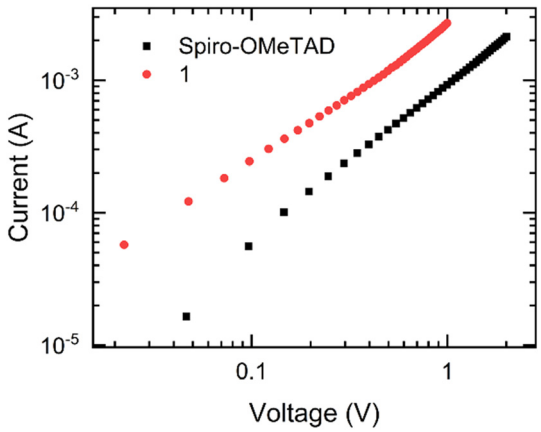

Fig. 5 Current(I)–voltage (V) characteristics of **Spiro-OMeTAD**, and **1**.

9.78×10^{15} photons per second). Fig. 6(a) shows **1** display a powder pattern shape EPR signal with the corresponding g value 2.007 consistent with the formation of the TPA radical cation of **1**. This is similar to prior work, although the radicals generated by **1** after 16 h of irradiation are much lower in quantity (0.11%, 0.12% for two separate trials).[30] Further details of the EPR experiment and methods used to estimate the radical concentration can be found in the ESI.† The radicals of **1** exhibit comparable EPR spectra even after 22 days in the dark without UV irradiation, which indicates their persistence and long lifetime (Fig. S25, ESI†). In comparison, **2** does not form appreciable amounts of radicals, as indicated by similar pre- and post-UV irradiated EPR spectra (Fig. S26, ESI†). These results suggest that reverse electron transfer is much slower for **1** as compared to **2**. The extensive $\pi\cdots\pi$ stacking interactions in **1** helps to delocalize the charges and persistent radicals may hinder charge transport manifested by lower conductivity values upon UV irradiation.

To further understand how the radical generation modulates the overall electronic properties of the crystals, occupied electronic states below the Fermi level of **1** were compared pre- and post-UV (365 nm) irradiation (Fig. 6(b)) in an *in situ* XPS experiment. To show the changing contribution of UV irradiation we compare the binding energies of the valence band maxima (VBM) – their distance below the Fermi level. After UV irradiation, we observe a shift in the VBM binding energy from 0.5 eV to 1.9 eV. The shift of VBM to higher binding energy

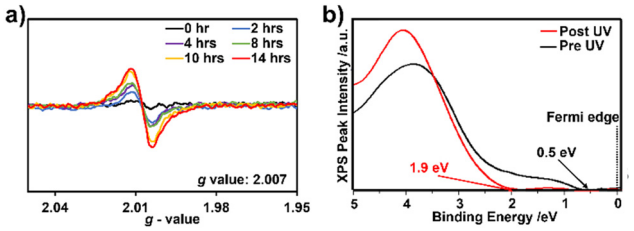

Fig. 6 (a) EPR data for the urea tethered TPA **1**. EPR spectra over time of UV irradiation. (b) XPS data in the valence band region for **1** recorded with a monochromatic Al Kα X-ray source.

could be expected upon compensation of dopants acting as acceptors in a p-type semiconductor.[55] One possible explanation could be the photogenerated intrinsic radicals act as donors, which suggests these materials to be potentially an organic semiconductor whose properties can be modified without the addition of extrinsic dopant impurities.

TD-DFT analysis of the electron transfer

Next, to gain insight into the electron transfer in the ground states, we turned to the TD-DFT based on the CAM-B3LYP[40] functional paired with the LANL2DZdp basis set, a combination proven adequate for the electronic coupling calculations for a similar series of derivatives. Further computational details are given in the ESI.† The frontier orbitals (HOMOs/LUMOs), their energies, and the gaps for **1**, **2**, and **3** are presented in Fig. 7.

First, we compare the energy levels to investigate the relationship between the molecular structure and the electronic properties. Introduction of the urea motif increases the HOMO (−6.503 eV, −6.585 eV,) and LUMO (−0.489 eV, −0.462 eV,) energy for **1**, **2** respectively compared to control **3**, −7.066 eV (HOMO) and −1.156 eV (LUMO). Overall, the HOMO–LUMO energy gap was higher in **1** (6.013 eV), and **2** (6.122 eV) compared to **3** (5.910 eV). In addition, as seen in Fig. 7 the frontier orbitals of **3** are delocalized over the entire molecular skeleton. In the hydrogen-bonded dimers of **1** and **2**, the electron density distribution is localized in either of the TPA units for the HOMO−1 and HOMO. In the case of LUMO and LUMO+1, the electron density is localized on the same TPA unit and methylene urea for **2**, while in **1** the electron density is distributed over the TPA unit and over a single unit of urea.

To further explore the possible pathways of electron transfer, we computed the fragment charge difference (FCD)[56] for four feasible pathways of **2** within the dimer model (Fig. S30, ESI†). The FCD schemes are useful for calculating electronic coupling between charged fragments. The FCD was obtained for the dimer model listed in Table S13 (ESI†). The dimer models i, iii, and iv all showed non-zero FCD while models i and iv gave similar FCD values ($dQ \sim 0.08$ a.u.). The electron transfer was further proved by invoking Koopman's theorem to calculate electronic coupling in the ground state for the dimer models i and iv of **2** and dimer models i and iii of **1**. As summarized in Tables S14 and 15 (ESI†), electronic coupling in **2** models was three times stronger than the dimer models of **1** (Fig. S31, ESI†). Since a higher electronic coupling correlates with higher electrical conductivity, the computed results are in agreement with the experimentally observed electrical conductivity values, which are higher for **2** than for **1**. A similar calculation performed for the dimer model of **2** as the radical cation yielded a significant decrease in coupling values (Table S16, ESI†). Thus, we argue that the conductivity is associated with the neutral dimers.

For additional insight into the electronic excitations, the UV-vis spectra in solution and in the solid-state were computed using the TD-DFT (CAM-B3LYP/LANL2DZdp) method within the random phase approximation (RPA). Further computational details can be found in the ESI.† Overall, the computed

 This journal is © the Owner Societies 2022

Open Access Article. Published on 18 July 2022. Downloaded on 5/10/2026 2:54:14 PM.
This article is licensed under a Creative Commons Attribution 3.0 Unported Licence.

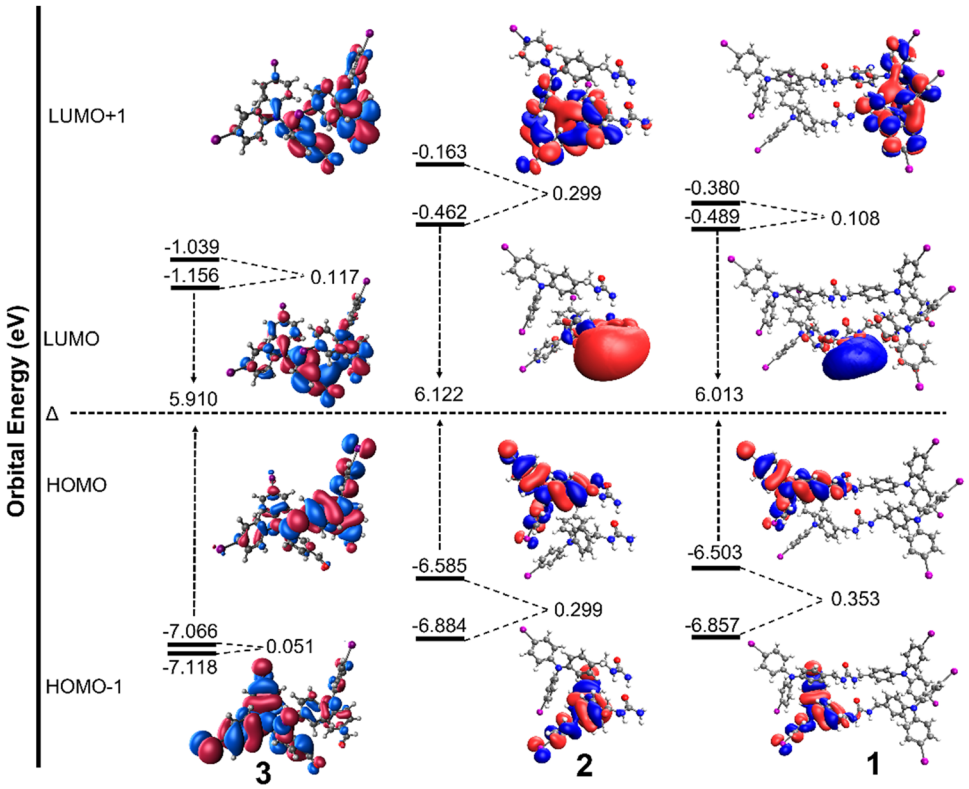

Fig. 7 From left, Frontier molecular orbitals, their energies, and gap of dimer of **3** with no hydrogen bonded groups and hydrogen bonded dimer of **2**, **1**. Frontier molecular orbitals generated using CAM-B3LYP/LANL2DZdp methods in the gas phase visualized at Isovalue 0.04.

absorption spectra are a good match with experimental diffuse reflectance spectra, as seen in Fig. S29(a) (ESI†). The highest occupied natural transition orbital (HONTO) and the lowest unoccupied natural transition orbital (LUNTO), shown in Fig. S29(b) (ESI†) were generated at the λ_{max} for the transitions with the highest oscillator strength which may explain the spatial overlap of frontier orbitals upon formation of radical cations. The electronic transitions and the corresponding wavelength are **1** (S_{30}, 361 nm), **2** (S_{27}, 367 nm), and **3** (S_{14}, 445 nm). The character of the spatial overlap of the NTOs suggests that these transitions are raised by $\pi\pi^*$ excitation. The key difference between these NTOs is that in **3**, with no hydrogen bonding groups, the electron density is distributed on only one of the TPA units. TPA **2** which forms an interchain hydrogen bond and a bifurcated hydrogen bond shows electron density in one of the TPA units which partially overlaps with the neighboring TPA. TPA **1**, with TPA on both sides of urea, shows delocalization of the electron density for just one of the TPA units. Both **1** and **2** lack electron density in the hydrogen bond motif urea which suggests that urea is important for spatial organization but doesn't directly contribute to frontier orbitals.

Conclusions

While much effort has been made to design and synthesize TPA-based conductors, true rational design remains a challenge due to insufficient understanding of the relationship between the supramolecular structure and properties. TPA derivatives have an intrinsic tendency to form amorphous glass structures that complicate the correlation of electronic properties and structures. To remove this constraint, we have incorporated urea, a directional hydrogen bonding motif that directs the self-assembly of the TPA, into ordered crystalline structures, forming needle shaped single crystals, readily amenable to SC-XRD analysis.

Two urea tethered TPA derivatives were synthesized and crystallized. While bifurcated urea–urea hydrogen bonding interactions guided the assembly, the close packing of the TPA units was promoted by halogen bonding and aryl stacking interactions (I–I, I–π, and π–π interactions). The conductivity of TPA **1** and **2** was measured by two contact probe methods where **2** shows higher conductivity values compared to **1**. Photoirradiation affects the overall electronic properties of the crystals and generates detectable though minor quantities of radicals. Moreover, we also observed that the decrease in conductivity values upon UV irradiation was much larger in **1** compared to **2**. Radical generation in these systems may be indicative of the formation of long-lived trapped states, although more studies are needed to elucidate the relationship of such traps to electronic transport. A comparison of valence XPS spectra before and after UV irradiation revealed a significant shift in VBM from 0.5 eV to 1.9 eV. These findings suggest that, despite their small quantity, the radicals produced can act as dopants,

Open Access Article. Published on 18 July 2022. Downloaded on 5/10/2026 2:54:14 PM.
This article is licensed under a Creative Commons Attribution 3.0 Unported Licence.

potentially aiding the design of dopant free hole transporter materials. According to the TD-DFT calculations, a urea-directed assembly is important for transferring the electrons while the close packing of TPA units promote hole mobilities. We hypothesize that continuous π stacking interactions help to delocalize the electron distribution facilitating the charge transport. Measurements of the conductivity of **1** in thin films have shown an increase upon addition of LiTFSI and tBP, yielding a favorable comparison to the popular hole-carrying material Spiro-OMeTAD. Collectively, these findings will aid in the development of TPA control assemblies and next-generation TPA-based functional materials for optoelectronic applications.

Author contributions

LSS initiated the study. FA, PD, SG, AG, MSH, NP, LSS planned experiments, analyzed data, and wrote the manuscript. FA, SG, MSH, SGK, MDS performed experiments and/or calculations. All authors contributed to the data analysis and to the final version of the manuscript.

Conflicts of interest

There are no conflicts to declare.

Acknowledgements

This work was supported in part by the National Science Foundation CHE-1904386 (LSS) and OIA-1655740 (LSS, ABG, SG). Computational work for MSH was also supported in part by the U.S. Department of Energy, Office of Science, Office of Basic Energy Sciences Separation Science program under Award Number DE-SC0020272. SG acknowledges partial support from the National Science Foundation under Grants CHE-1955768 and OIA-1655740 and a GEAR-CRP 20GC03 award. PD and NP acknowledge support from the UK's Engineering and Physical Sciences Research Council under award number EP/T010568/1.

References

1 M. B. Mills, T. Wohlhauser, B. Stein, W. R. Verduyn, E. Song, P. Dechambenoit, M. Rouzières, R. Clérac and K. E. Preuss, *J. Am. Chem. Soc.*, 2018, **140**, 16904–16908.
2 M. Liu, L. Zhang and T. Wang, *Chem. Rev.*, 2015, **115**, 7304–7397.
3 F. Würthner, C. R. Saha-Möller, B. Fimmel, S. Ogi, P. Leowanawat and D. Schmidt, *Chem. Rev.*, 2016, **116**, 962–1052.
4 P. Blanchard, C. Malacrida, C. Cabanetos, J. Roncali and S. Ludwigs, *Polym. Int.*, 2019, **68**, 589–606.
5 P. Agarwala and D. Kabra, *J. Mater. Chem. A*, 2017, **5**, 1348–1373.
6 M. L. Petrus, K. Schutt, M. T. Sirtl, E. M. Hutter, A. C. Closs, J. M. Ball, J. C. Bijleveld, A. Petrozza, T. Bein, T. J. Dingemans, T. J. Savenije, H. Snaith and P. Docampo, *Adv. Energy Mater.*, 2018, **8**, 1801605.
7 J. Zhao, Z. Yang, X. Chen, Z. Xie, T. Liu, Z. Chi, Z. Yang, Y. Zhang, M. P. Aldred and Z. Chi, *J. Mater. Chem. C*, 2018, **6**, 4257–4264.
8 X. Hai, Z. Guo, X. Lin, X. Chen and J. Wang, *ACS Appl. Mater. Interfaces*, 2018, **10**, 5853–5861.
9 S. Roquet, A. Cravino, P. Leriche, O. Alévêque, P. Frère and J. Roncali, *J. Am. Chem. Soc.*, 2006, **128**, 3459–3466.
10 E. Moulin, F. Niess, M. Maaloum, E. Buhler, I. Nyrkova and N. Giuseppone, *Angew. Chem., Int. Ed.*, 2010, **49**, 6974–6978.
11 V. Faramarzi, F. Niess, E. Moulin, M. Maaloum, J. F. Dayen, J. B. Beaufrand, S. Zanettini, B. Doudin and N. Giuseppone, *Nat. Chem.*, 2012, **4**, 485–490.
12 Y. Domoto, E. Busseron, M. Maaloum, E. Moulin and N. Giuseppone, *Chem. – Eur. J.*, 2015, **21**, 1938–1948.
13 R. Hussain, M. Y. Mehboob, M. U. Khan, M. Khalid, Z. Irshad, R. Fatima, A. Anwar, S. Nawab and M. Adnan, *J. Mater. Sci.*, 2021, **56**, 5113–5131.
14 H. Li, K. Fu, P. P. Boix, L. H. Wong, A. Hagfeldt, M. Grätzel, S. G. Mhaisalkar and A. C. Grimsdale, *ChemSusChem*, 2014, **7**, 3420–3425.
15 M. L. Petrus, K. Schutt, M. T. Sirtl, E. M. Hutter, A. C. Closs, J. M. Ball, J. C. Bijleveld, A. Petrozza, T. Bein, T. J. Dingemans, T. J. Savenije, H. Snaith and P. Docampo, *Adv. Energy Mater.*, 2018, **8**, 1801605.
16 A. H. Flood, J. F. Stoddart, D. W. Steuerman and J. R. Heath, *Science*, 2004, **306**, 2055–2056.
17 H. Chen and J. Fraser Stoddart, *Nat. Rev. Mater.*, 2021, **6**, 804–828.
18 C. Chen, H. Li, X. Ding, M. Cheng, H. Li, L. Xu, F. Qiao, H. Li and L. Sun, *ACS Appl. Mater. Interfaces*, 2018, **10**, 38970–38977.
19 M. Fahlman, S. Fabiano, V. Gueskine, D. Simon, M. Berggren and X. Crispin, *Nat. Rev. Mater.*, 2019, **4**, 627–650.
20 I. Nyrkova, E. Moulin, J. J. Armao, M. Maaloum, B. Heinrich, M. Rawiso, F. Niess, J. J. Cid, N. Jouault, E. Buhler, A. N. Semenov and N. Giuseppone, *ACS Nano*, 2014, **8**, 10111–10124.
21 E. Busseron, J. J. Cid, A. Wolf, G. Du, E. Moulin, G. Fuks, M. Maaloum, P. Polavarapu, A. Ruff, A. K. Saur, S. Ludwigs and N. Giuseppone, *ACS Nano*, 2015, **9**, 2760–2772.
22 A. Perumal, H. Faber, N. Yaacobi-Gross, P. Pattanasattayavong, C. Burgess, S. Jha, M. A. McLachlan, P. N. Stavrinou, T. D. Anthopoulos, D. D. C. Bradley, A. Perumal, H. Faber, N. Yaacobi-Gross, P. Pattanasattayavong, S. Jha, P. N. Stavrinou, T. D. Anthopoulos, D. D. C. Bradley, C. Burgess and M. A. McLachlan, *Adv. Mater.*, 2015, **27**, 93–100.
23 Y. E. Kim, A. Ko, H. J. Jang, S. J. Yoon, S. H. Roh, J. Y. Lee, J. Y. Lee, D. Kim, J. K. Kim and K. S. Yook, *Dyes Pigm.*, 2021, **187**, 109122.
24 M. R. Nagar, A. Choudhury, D. Tavgeniene, R. Beresneviciute, D. Blazevicius, V. Jankauskas, K. Kumar, S. Banik, S. Ghosh, S. Grigalevicius and J. H. Jou, *J. Mater. Chem. C*, 2022, **10**, 3593–3608.
25 D. Shi, X. Qin, Y. Li, Y. He, C. Zhong, J. Pan, H. Dong, W. Xu, T. Li, W. Hu, J. L. Brédas and O. M. Bakr, *Sci. Adv.*, 2016, **4**, 1501491.

Open Access Article. Published on 18 July 2022. Downloaded on 5/10/2026 2:54:14 PM.
This article is licensed under a Creative Commons Attribution 3.0 Unported Licence.

26 J. J. Armao, P. Rabu, E. Moulin and N. Giuseppone, *Nano Lett.*, 2016, **16**, 2800–2805.
27 A. J. Sindt, M. D. Smith, S. Berens, S. Vasenkov, C. R. Bowers and L. S. Shimizu, *Chem. Commun.*, 2019, **55**, 5619–5622.
28 L. S. Shimizu, S. R. Salpage and A. A. Korous, *Acc. Chem. Res.*, 2014, **47**, 2116–2127.
29 D. W. Goodlett, A. J. Sindt, M. S. Hossain, R. Merugu, M. D. Smith, S. Garashchuk, A. D. Gudmundsdottir and L. S. Shimizu, *J. Phys. Chem. A*, 2021, **125**, 1336–1344.
30 M. S. Hossain, A. J. Sindt, D. W. Goodlett, D. J. Shields, C. J. O'Connor, A. Antevska, S. G. Karakalos, M. D. Smith, S. Garashchuk, T. D. Do, A. D. Gudmundsdottir and L. S. Shimizu, *J. Phys. Chem. C*, 2021, **125**, 19991–20002.
31 Z. Li, Q. Dong, B. Xu, H. Li, S. Wen, J. Pei, S. Yao, H. Lu, P. Li and W. Tian, *Sol. Energy Mater. Sol. Cells*, 2011, **95**, 2272–2280.
32 Z. Li, T. Ye, S. Tang, C. Wang, D. Ma and Z. Li, *J. Mater. Chem. C*, 2015, **3**, 2016–2023.
33 H. Tian, X. Yang, R. Chen, R. Zhang, A. Hagfeldt and L. Sun, *J. Phys. Chem. C*, 2008, **112**, 11023–11033.
34 G. G. Dubinina, R. S. Price, K. A. Abboud, G. Wicks, P. Wnuk, Y. Stepanenko, M. Drobizhev, A. Rebane and K. S. Schanze, *J. Am. Chem. Soc.*, 2012, **134**, 19346–19349.
35 Y. Shao, *et al.*, *Mol. Phys.*, 2015, **113**, 184–215.
36 *Spartan'18 (version 1.4.4)*, Wavefunction, Inc., Irvine, CA, 2019.
37 B. P. Pritchard, D. Altarawy, B. Didier, T. D. Gibson and T. L. Windus, *J. Chem. Inf. Model.*, 2019, **59**, 4814–4820.
38 F. J. Devlin, J. W. Finley, P. J. Stephens and M. J. Frisch, *J. Phys. Chem.*, 1995, **99**, 16883–16902.
39 R. Ditchfield, W. J. Hehre and J. A. Pople, *J. Chem. Phys.*, 1971, **54**, 724–728.
40 T. Yanai, D. P. Tew and N. C. Handy, *Chem. Phys. Lett.*, 2004, **393**, 51–57.
41 P. J. Hay and W. R. Wadt, *J. Chem. Phys.*, 1985, **82**, 270–283.
42 K. A. Peterson, D. Figgen, E. Goll, H. Stoll and M. Dolg, *J. Chem. Phys.*, 2003, **119**, 11113–11123.
43 A. Bondi, *J. Phys. Chem.*, 1964, **68**, 441–451.
44 J. J. Armao, M. Maaloum, T. Ellis, G. Fuks, M. Rawiso, E. Moulin and N. Giuseppone, *J. Am. Chem. Soc.*, 2014, **136**, 11382–11388.
45 M. A. Spackman and D. Jayatilaka, *CrystEngComm*, 2009, **11**, 19–32.
46 J. F. Moulder, W. F. Stickle, P. E. Sobol, K. D. Bomben and J. Chastain, *Handbook of X-ray Photoelectron Spectroscopy: A Reference Book of Standard Spectra for Identification and Interpretation of XPS Data*, PerkinElmer Corporation, United States of America, 1992.
47 B. Som, S. R. Salpage, J. Son, B. Gu, S. G. Karakalos, M. D. Smith and L. S. Shimizu, *CrystEngComm*, 2017, **19**, 484–491.
48 X. Du, B. Liu, L. Li, X. Kong, C. Zheng, H. Lin, Q. Tong, S. Tao and X. Zhang, *J. Mater. Chem. A*, 2018, **6**, 23840–23855.
49 Y. Li, H. Li, C. Zhong, G. Sini and J.-L. Brédas, *npj Flexible Electron.*, 2017, **1**, 1–8.
50 A. Abate, T. Leijtens, S. Pathak, J. Teuscher, R. Avolio, M. E. Errico, J. Kirkpatrik, J. M. Ball, P. Docampo, I. McPherson and H. J. Snaith, *Phys. Chem. Chem. Phys.*, 2013, **15**, 2572–2579.
51 W. H. Nguyen, C. D. Bailie, E. L. Unger and M. D. McGehee, *J. Am. Chem. Soc.*, 2014, **136**, 10996–11001.
52 A. Abate, T. Leijtens, S. Pathak, J. Teuscher, R. Avolio, M. E. Errico, J. Kirkpatrik, J. M. Ball, P. Docampo, I. Mcpherson and H. J. Snaith, *Phys. Chem. Chem. Phys.*, 2013, **15**, 2572.
53 E. J. Juarez-Perez, M. R. Leyden, S. Wang, L. K. Ono, Z. Hawash and Y. Qi, *Chem. Mater.*, 2016, **28**, 5702–5709.
54 L. Caliò, M. Salado, S. Kazim and S. Ahmad, *Joule*, 2018, **2**, 1800–1815.
55 A. D. Scaccabarozzi, A. Basu, F. Aniés, J. Liu, O. Zapata-Arteaga, R. Warren, Y. Firdaus, M. I. Nugraha, Y. Lin, M. Campoy-Quiles, N. Koch, C. Müller, L. Tsetseris, M. Heeney and T. D. Anthopoulos, *Chem. Rev.*, 2022, **122**, 4420–4492.
56 A. A. Voityuk and N. Rösch, *J. Chem. Phys.*, 2002, **117**, 5607.